PHYSICAL REVIEW VOLUME 182, NUMBER 3 15 JUNE 1969

Energy-Band Structure and Electronic Properties of SnTe

Sohrab Rabii
Monsanto Company, St. Louis, Missouri 63166
(Received 23 December 1968)

The energy-band structure of SnTe is calculated using the augmented-plane-wave method, taking into account the relativistic corrections. The resulting wave functions at L are used to calculate momentum matrix elements. These matrix elements are then used in a $\mathbf{k}\cdot\mathbf{p}$ perturbation calculation in the presence of a magnetic field to obtain band parameters at point L in the Brillouin zone. Nonparabolic expansions for the conduction and valence bands at L are obtained using Cohen's model. The effect of strain on the energy levels at L is calculated using the deformation-potential theory. The results indicate a complicated shape for the valence band at L, with two maxima at each side of L on the face of the Brillouin zone. A record set of apparent maxima is found in the Σ direction at $\mathbf{k}=(\pi/a)(\frac{4}{5}, \frac{4}{5}, 0)$. This is consistent with the "two-valence-band" model suggested to explain the experimental results. We are investigating the possibility that these extrema may be saddle points. The conduction- and valence-band-edge symmetries at L are opposite to those of the lead chalcogenides, as are the band-gap deformation potentials at this point (-8.68 eV for SnTe and 11.55–17.24 eV for the others). This is in agreement with the experimentally proposed "band-inversion" model.

I. INTRODUCTION

In recent years, a large body of experimental information on the properties of SnTe has been accumulated. These results have led to a great deal of fragmentary information about the electronic structure of this material. However, there have been only two theoretical investigations of SnTe. Lin *et al.*[1] have carried out an energy-band calculation using the "empirical pseudopotential" method and have obtained the imaginary part of the frequency-dependent dielectric function. Herman *et al.*[2] have recently employed the orthogonal-plane-wave (OPW) method at several points in the Brillouin zone, coupled with an interpolation scheme to connect these points together. They worked directly with a relativistic wave equation at six points in the zone and made identifications of their theoretically allowed transitions with optical and electroreflectivity data. In the present work, energy levels and wave functions are calculated at 12 points in the Brillouin zone, which leads to the most detailed picture of the bands so far obtained. The wave functions are then used to calculate matrix elements of momentum and strain at L, resulting in effective masses, g factors, and deformation potentials at this point.

The first-principles augmented-plane-wave (APW) method has been used successfully in a similar study of the lead chalcogenides, which have the same crystal structure (fcc-NaCl) as SnTe. This consideration, along with the availability of the computer codes, led to the choice of this method for the present work. The details of the APW method and of the Hamiltonian which is used are given elsewhere.[3,4] The unperturbed calculation, which uses only the potential and the kinetic energy terms, is followed by two successive perturbations referred to as "relativistic perturbations," which add the mass-velocity, Darwin, and the spin-orbit interaction terms to the Hamiltonian. Because of computational limitations, the wave functions in the relativistic perturbation in case of the lead chalcogenides[3–5] were limited to 10 APW's. At points of high symmetry, this number is quite sufficient to achieve satisfactory convergence. This is not necessarily true at points on lower symmetry lines. The early work on SnTe,[6] with only 10 APW's in the relativistic functions, in fact, led to a spurious set of maxima in the valence band in [111] directions. The relativistic program was then modified to accommodate up to 20 APW's. This modification led to the disappearance of the spurious maxima and to shifts of up to 0.5 eV in the Δ direction. The wave functions are used to calculate matrix elements of momentum and deformation potentials at L. The momentum matrix elements are then used in a $\mathbf{k}\cdot\mathbf{p}$ perturbation to obtain effective masses and g factors at L. Cohen's nonparabolic model is applied to the conduction and valence bands at L, and new values for the effective masses are obtained. The experiments on Hall effect, thermoelectric power, optical properties, Shubnikov–de Haas measurements, and superconductivity led to proposed models for the electronic processes in SnTe. These models are discussed in the light of the informations supplied by the present work on the symmetries and positions of various band extrema and their calculated parameters.

II. ENERGY BANDS

The crystal potential used is of the familiar muffin-tin type which includes the Slater free-electron exchange. The contributions of up to the second nearest neighbors are included. Table I gives the numerical

---

[1] P. J. Lin, W. Saslow, and M. L. Cohen, Solid State Commun. **5**, 893 (1967).

[2] F Herman, R L. Kortum, I. B. Ortenburger, and J. P. Van Dyke, J. Phys. Radium (to be published).

[3] J. B. Conklin, Jr., L. E. Johnson, and G. W. Pratt, Jr., Phys. Rev. **137**, A1282 (1965).

[4] S. Rabii, Phys. Rev. **167**, 801 (1968).

[5] L. E. Johnson, J. B. Conklin, Jr., and G. W. Pratt, Jr., Phys. Rev. Letters **11**, 538 (1963).

[6] S. Rabii, Bull. Am. Phys. Soc. **13**, 413 (1968).

TABLE I. Numerical values in atomic units for some of the constants involved in the calculation.

Lattice parameter a	11.9016
Radius of Sn sphere	2.9484
Radius of Te sphere	3.0024
Constant potential outside spheres	−1.0156

values for some of the constants involved in the calculation. The energy bands are calculated in the three important directions [111], [010], and [110] (Fig. 1). The energy levels at L, which correspond to the valence and conduction bands, have L_6^- and L_6^+ symmetries, respectively, which is the reverse of the lead chalcogenides.[3,4] There is another set of apparent maxima in valence band in the [110] direction, which is 0.3 eV above the L_6^- level. Although this indicates an indirect gap, it is possible, owing to sensitivity of the L_6^- level to small changes in the constant potential in the region outside the sphere (hereafter referred to as V_c), that for a different choice of this parameter the L_6^- maxima will actually be above the Σ_5. Furthermore, as we shall see later, the $\mathbf{k}\cdot\mathbf{p}$ perturbation indicates that the actual maxima are not at L but very near to it on the face of the Brillouin zone in the direction perpendicular to the [111]. These two humps may, even with the present choice of V_c, be above the Σ_5 level. The possibility should be borne in mind, as pointed out by Herman *et al.*,[2] that the [110] extrema may turn out to be saddle points. However, in the absence of any concrete evidence for this and in view of the strong experimental evidence for the existence of a second valence band (Sec. V C), this possibility is set aside pending the outcome of our continuing investigations.

In order to study the effect of V_c on the energy levels at L, these levels are calculated for four different values of this parameter (Fig. 2). If we put the L_6^- level aside, the rest of the levels shift together, so that the various gaps are preserved. The upward motion, to a great extent, is simply a reflection of the change of the reference point which is V_c. However, the L_6^- level moves down and this leads not only to change in the size of the gap but also to a reversal of the order of the L_6^- and L_6^+ levels. The sensitivity of L_6^- to changes in V_c is due to the nature of its charge density. Table II gives charge density distribution for the three points under consideration. Almost 52% of the charge for the L_6^- level is in the constant potential region, so that its position will change drastically with a change in V_c. The L_6^- level lacks any appreciably S-type charge distribution.

The value of −1.0156 for V_c was obtained by averaging the crystal potential in the region outside the spheres. Any change in its value will be in a direction to raise L_6^- towards L_6^+ level. Thus it is open question whether the gap is at L or between Σ and L. The calculated values of the energies at different points in the Brillouin zone along with the relativistic corrections are tabulated in Table III.

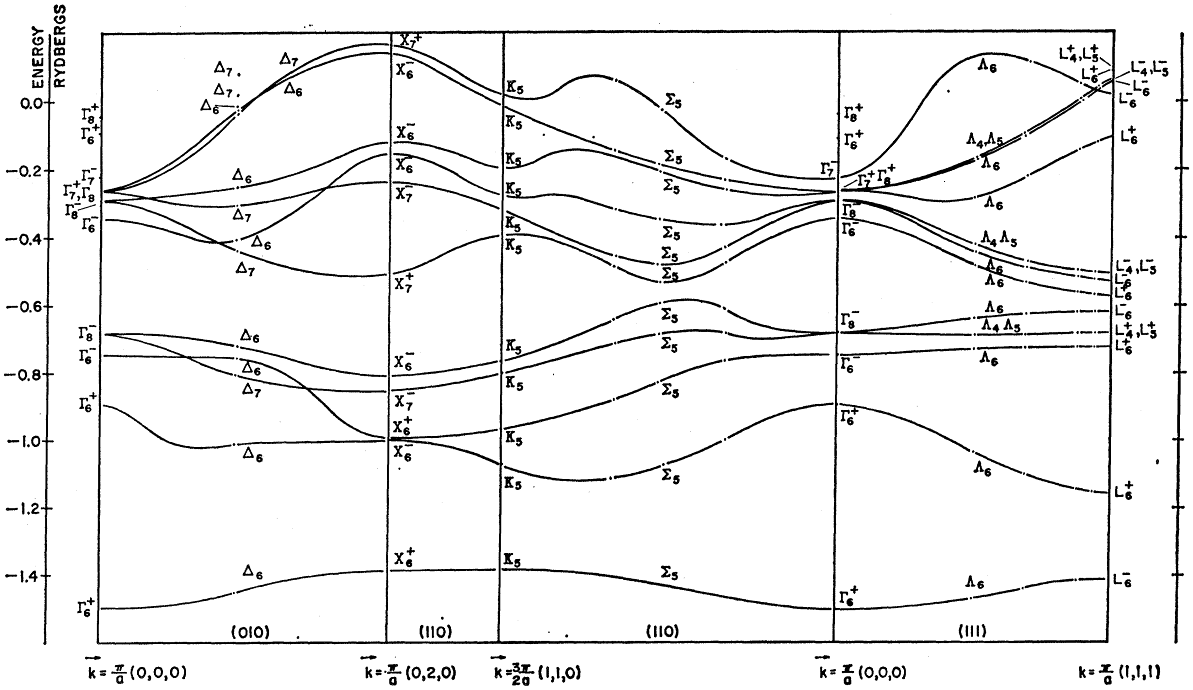

FIG. 1. Energy bands for SnTe in the [111], [010], and [110] directions.

III. k·p PERTURBATION

A **k**·**p** perturbation is applied to the L_6^- and L_6^+ levels corresponding to the valence and conduction bands to calculate an E-versus-**k** expansion for these bands and thus obtain effective masses and g factors. Following the formalisms of Luttinger and Kohn,[7] and Roth,[8] and the notation of Ref. 4, the matrix element of the effective Hamiltonian in the presence of a magnetic field is given by

$$\langle\Phi_{n\kappa i}|\mathcal{H}_{\mathrm{eff}}|\Phi_{n\kappa j}\rangle=\left(E_n{}^0+\frac{\hbar^2\kappa^2}{2m}\right)\delta_{ij}+\boldsymbol{\kappa}\cdot\sum_\mu\frac{\{\boldsymbol{\pi}_{i\mu}\cdot\boldsymbol{\pi}_{\mu j}\}}{E_n{}^0-E_\mu{}^0}\cdot\boldsymbol{\kappa}$$
$$+2\mu_\beta S_{ij}\cdot\mathbf{H}-\frac{ie\hbar}{2m^2c}\mathbf{H}\cdot\sum_\mu\frac{\boldsymbol{\pi}_{i\mu}\times\boldsymbol{\pi}_{\mu j}}{E_n{}^0-E_\mu{}^0},\quad(1)$$

where

$$\boldsymbol{\pi}=\mathbf{p}+(\hbar/4mc^2)\boldsymbol{\sigma}\times(\boldsymbol{\nabla}V)-(2m^2c^2)^{-1}(p^2)\mathbf{p}$$
$$-(2m^2c^2)^{-1}(\mathbf{P}\cdot\mathbf{p})\mathbf{p}-(4m^2c^2)^{-1}(p^2)\mathbf{P}.\quad(2)$$

Figure 3 shows the energy levels that enter into the **k**·**p** calculation. Only the levels denoted by numbers 1–4 and letters c and v are included in the sum over μ in Eq. (1), since the energy separation of the rest of the levels from the conduction-valence-band complex is of the order of 0.4 Ry or larger. However, because of spin-orbit mixing, all these levels enter into the composition of each other and must be taken into account. Tables IV and V give the spin-orbit mixing of the levels included in the sum over μ in Eq. (1). Since there is more than one single group level of the same symmetry, a second subscript is used to distinguish these levels. This subscript coincides with the numbering of the spinor function, in the spin-orbit seculare quation, which arises from the particular single-group level. Thus $M_{19,34}{}^v$ is the matrix element of $2\pi_y$ between L_1 level, which gives rise to ninth spinor function, and the L_3', which gives rise to the fourth spinor function.

TABLE II. Charge-density distribution of three important levels in the Brillouin zone.

	Plane-wave region	$l=0$		$l=1$		$l=2$		$l=3$	
		Sn	Te	Sn	Te	Sn	Te	Sn	Te
L_6^+	0.280	0.388	0.000	0.000	0.263	0.038	0.000	0.000	0.031
L_6^-	0.515	0.000	0.169	0.226	0.000	0.000	0.072	0.018	0.000
Σ_6	0.342	0.185	0.019	0.174	0.196	0.019	0.046	0.006	0.014

The relationships between the single-group matrix elements are given in Ref. 4. These matrix elements are then used to obtain the double-group matrix elements of $\boldsymbol{\pi}$ operator between the final spin-orbit-mixed levels (Tables VI and VII). The matrix elements not listed are either zero or can be obtained from those given by application of the time-reversal operator and the point-group symmetry of the group of k vector. The Slater system of atomic units is used. For computational ease, the matrix elements of $\boldsymbol{\pi}/m=2\boldsymbol{\pi}$ are calculated instead of $\boldsymbol{\pi}$.

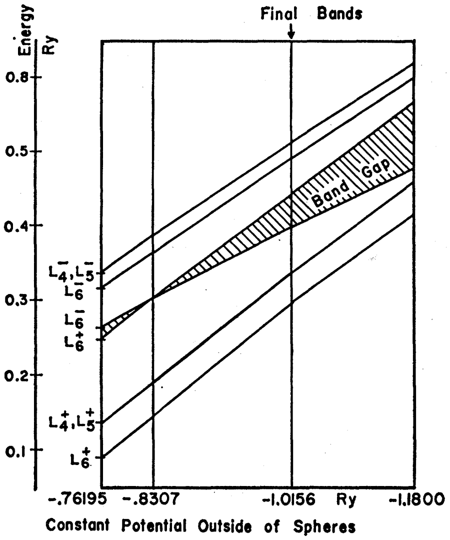

FIG. 2. Variation of the energy levels at L with change in the constant potential outside the APW spheres.

The resulting matrix elements of the effective Hamiltonian in the presence of magnetic field for $|L_6^-,v\rangle$ and $|L_6^+,c\rangle$ levels are

$$\langle L_{61}^-,v|\mathcal{H}_{\mathrm{eff}}|L_{61}^-,v\rangle=E(L_6^-,v)+(\hbar^2/2m)$$
$$\times[-0.42\kappa_z{}^2+14.14(\kappa_x{}^2+\kappa_y{}^2)]$$
$$-\tfrac{1}{2}\mu_\beta(7.50)H_z,\quad(3)$$

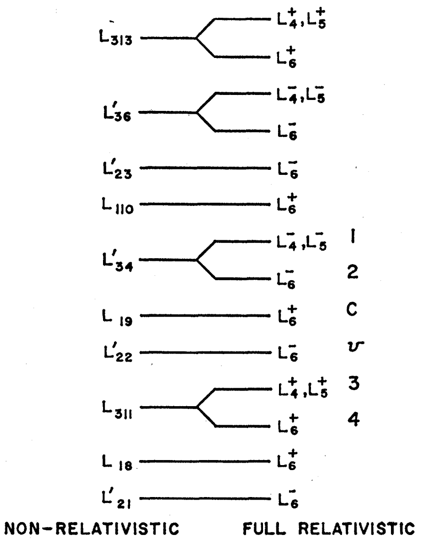

FIG. 3. Energy levels taken into account for **k**·**p** perturbation. Only the levels marked as 1–4, c, and v are used in the sum over μ in Eq. (1).

---

[7] J. M. Luttinger and W. Kohn, Phys. Rev. **97**, 869 (1955).

[8] L. M. Roth, Phys. Rev. **118**, 1534 (1960).

TABLE III. The calculated energy levels for SnTe in units of Ry. E_{NR}, E_R', and E_R are the eigenvalues for the nonrelativistic, relativistic without spin-orbit interaction, and the full relativistic Hamiltonians, respectively. The wave vectors are in units of π/a.

Level	E_{NR}	E_R'	E_R		Level	E_{NR}	E_R'	E_R		Level	E_{RN}	E_R'	E_R	
		(a)					(b)					(c)		
$\Gamma(0,0,0)$					$\Lambda(\frac{1}{2},\frac{1}{2},\frac{1}{2})$					$\Sigma(\frac{1}{2},\frac{1}{2},0)$				
Γ_{12}	−0.029	−0.039	−0.039	Γ_8^+	Λ_3	−0.156	−0.166	−0.165	Λ_4,Λ_5	Σ_1	−0.120	−0.168	−0.168	Σ_5
Γ_1	−0.034	−0.111	−0.111	Γ_6^+				−0.168	Λ_6	Σ_2	−0.227	−0.234	−0.234	Σ_5
Γ_2'	−0.230	−0.230	−0.230	Γ_7^-	Λ_1	−0.262	−0.283	−0.282	Λ_6	Σ_3	−0.225	−0.261	−0.261	Σ_5
Γ_{25}'	−0.257	−0.264	−0.264	Γ_8^+	Λ_3	−0.403	−0.436	−0.423	Λ_4,Λ_5	Σ_3	−0.346	−0.366	−0.366	Σ_5
			−0.264	Γ_7^+				−0.442	Λ_6	Σ_4	−0.401	−0.433	−0.431	Σ_5
Γ_{15}	−0.265	−0.308	−0.291	Γ_8^-	Λ_1	−0.415	−0.475	−0.481	Λ_6	Σ_1	−0.424	−0.473	−0.475	Σ_5
			−0.343	Γ_6^-	Λ_1	−0.563	−0.642	−0.637	Λ_6	Σ_1	−0.537	−0.613	−0.611	Σ_5
Γ_{15}	−0.655	−0.704	−0.684	Γ_8^-	Λ_3	−0.657	−0.704	−0.685	Λ_4,Λ_5	Σ_4	−0.634	−0.683	−0.685	Σ_5
			−0.743	Γ_6^-				−0.728	Λ_6	Σ_3	−0.719	−0.759	−0.759	Σ_5
Γ_1	−0.738	−0.894	−0.894	Γ_6^+	Λ_1	−0.941	−1.034	−1.034	Λ_6	Σ_1	−0.885	−1.009	−1.009	Σ_5
Γ_1	−1.409	−1.502	−1.502	Γ_6^+	Λ_1	−1.366	−1.466	−1.466	Λ_6					
		(d)					(e)					(f)		
$L(1,1,1)$					$\Lambda(\frac{7}{8},\frac{7}{8},\frac{7}{8})$					$\Sigma(\frac{4}{5},\frac{4}{5},0)$				
L_3	+0.108	+0.093	+0.097	L_4^+,L_5^+	Λ_1	+0.098	+0.056	+0.056	Λ_6	Σ_1	+0.014	−0.020	−0.019	Σ_5
			+0.090	L_6^+	Λ_3	+0.023	+0.010	+0.013	Λ_4,Λ_5	Σ_2	−0.179	−0.185	−0.185	Σ_5
L_3'	+0.087	+0.074	+0.077	L_4^-,L_5^-				+0.007	Λ_6	Σ_3	−0.170	−0.208	−0.208	Σ_5
			+0.072	L_6^-	Λ_1	−0.100	−0.137	−0.137	Λ_6	Σ_3	−0.322	−0.348	−0.348	Σ_5
L_2'	+0.062	+0.023	+0.022	L_6^-	Λ_3	−0.480	−0.509	−0.498	Λ_4,Λ_5	Σ_4	−0.448	−0.482	−0.480	Σ_5
L_1	−0.065	−0.103	−0.103	L_6^+				−0.518	Λ_6	Σ_1	−0.462	−0.534	−0.536	Σ_5
L_3'	−0.486	−0.515	−0.504	L_4^-,L_5^-	Λ_1	−0.480	−0.561	−0.560	Λ_6	Σ_1	−0.533	−0.597	−0.595	Σ_5
			−0.525	L_6^-	Λ_1	−0.562	−0.619	−0.620	Λ_6	Σ_4	−0.637	−0.685	−0.688	Σ_5
L_1	−0.485	−0.571	−0.568	L_6^+	Λ_3	−0.652	−0.698	−0.680	Λ_4,Λ_5	Σ_3	−0.794	−0.828	−0.828	Σ_5
L_2'	−0.562	−0.615	−0.617	L_6^-				−0.720	Λ_6	Σ_1	−0.974	−1.067	−1.067	Σ_5
L_3	−0.551	−0.698	−0.679	L_4^+,L_5^+	Λ_1	−1.081	−1.145	−1.145	Λ_6					
			−0.720	L_6^+	Λ_1	−1.300	−1.417	−1.417	Λ_6					
L_1	−1.095	−1.155	−1.155	L_6^+										
L_2'	−1.291	−1.411	−1.411	L_6^-										
		(g)					(h)					(i)		
$X(0,2,0)$					$\Lambda(\frac{11}{16},\frac{11}{16},\frac{11}{16})$					$\Sigma(1,1,0)$				
X_2	+0.180	+0.166	+0.166	X_7^+	Λ_1	+0.168	+0.119	+0.120	Λ_6	Σ_1	+0.097	+0.062	+0.062	Σ_5
X_4'	+0.174	+0.141	+0.142	X_6^-	Λ_3	−0.075	−0.086	−0.084	Λ_4,Λ_5	Σ_2	−0.135	−0.141	−0.141	Σ_5
X_4'	−0.054	−0.123	−0.120	X_6^-				−0.088	Λ_6	Σ_3	−0.122	−0.162	−0.162	Σ_5
X_5'	−0.137	−0.197	−0.158	X_6^-	Λ_1	−0.189	−0.220	−0.220	Λ_6	Σ_3	−0.285	−0.319	−0.319	Σ_5
			−0.238	X_7^-	Λ_3	−0.450	−0.481	−0.469	Λ_4,Λ_5	Σ_4	−0.425	−0.464	−0.462	Σ_5
X_3	−0.504	−0.509	−0.509	X_7^+				−0.489	Λ_6	Σ_1	−0.412	−0.481	−0.483	Σ_5
X_5'	−0.795	−0.831	−0.809	X_6^-	Λ_1	−0.455	−0.527	−0.529	Λ_6	Σ_1	−0.592	−0.651	−0.649	Σ_5
			−0.854	X_7^-	Λ_1	−0.561	−0.629	−0.626	Λ_6	Σ_4	−0.669	−0.713	−0.715	Σ_5
X_1	−0.894	−0.996	−0.996	X_6^+	Λ_3	−0.655	−0.701	−0.683	Λ_4,Λ_5	Σ_3	−0.843	−0.875	−0.875	Σ_5
X_4'	−0.970	−0.996	−0.998	X_6^-				−0.724	Λ_6	Σ_1	−1.016	−1.102	−1.102	Σ_5
X_1	−1.257	−1.385	−1.385	X_6^+	Λ_1	−1.022	−1.100	−1.100	Λ_6					
					Λ_1	−1.332	−1.440	−1.440	Λ_6					
		(j)					(k)					(l)		
$K(\frac{3}{2},\frac{3}{2},0)$					$\Lambda(\frac{15}{16},\frac{15}{16},\frac{15}{16})$					$\Delta(0,1,0)$				
K_2	+0.019	+0.014	+0.014	K_5	Λ_3	+0.059	+0.045	+0.048	Λ_4,Λ_5	Δ_2'	+0.084	+0.082	+0.082	Δ_7
K_3	+0.027	−0.012	−0.012	K_5				+0.043	Λ_6	Δ_2	+0.027	+0.018	+0.018	Δ_7
K_3	−0.148	−0.198	−0.198	K_5	Λ_1	−0.075	−0.115	−0.115	Λ_6	Δ_1	+0.026	−0.020	−0.019	Δ_6
K_1	−0.231	−0.287	−0.282	K_5	Λ_3	−0.484	−0.513	−0.502	Λ_4,Λ_5	Δ_5	−0.014	−0.030	−0.023	Δ_6
K_4	−0.272	−0.320	−0.324	K_5				−0.523	Λ_6				−0.036	Δ_7
K_1	−0.366	−0.394	−0.396	K_5	Λ_1	−0.483	−0.569	−0.567	Λ_6	Δ_5	−0.234	−0.280	−0.257	Δ_6
K_1	−0.709	−0.766	−0.762	K_5	Λ_1	−0.562	−0.619	−0.620	Λ_6				−0.303	Δ_7
K_4	−0.761	−0.799	−0.803	K_5	Λ_3	−0.651	−0.698	−0.679	Λ_4,Λ_5	Δ_1	−0.333	−0.408	−0.407	Δ_6
K_3	−0.937	−0.964	−0.964	K_5				−0.719	Λ_6	Δ_2'	−0.439	−0.444	−0.444	Δ_7
K_1	−1.006	−1.076	−1.076	K_5	Λ_1	−1.091	−1.153	−1.153	Λ_6	Δ_1	−0.661	−0.716	−0.716	Δ_6
K_1	−1.254	−1.383	−1.383	K_5						Δ_5	−0.739	−0.779	−0.754	Δ_6
													−0.808	Δ_7
										Δ_1	−0.904	−1.010	−1.010	Δ_6
										Δ_1	−1.351	−1.453	−1.453	Δ_6

$$\langle L_{61}{}^-,v|\mathcal{H}_{\mathrm{eff}}|L_{62}{}^-,v\rangle=-\tfrac{1}{2}\mu_\beta(5.62)H^-, \tag{4}$$

$$\langle L_{61}{}^+,c|\mathcal{H}_{\mathrm{eff}}|L_{61}{}^+,c\rangle=E(L_6{}^+,c)+(\hbar^2/2m)\times[2.34\kappa_z{}^2-23.42(\kappa_x{}^2+\kappa_y{}^2)]-\tfrac{1}{2}\mu_\beta(4.07)H_z, \tag{5}$$

$$\langle L_{61}{}^+,c|\mathcal{H}_{\mathrm{eff}}|L_{62}{}^+,c\rangle=\tfrac{1}{2}\mu_\beta(7.33)H^-, \tag{6}$$

where $H^\pm=H_x\pm iH_y$.

In view of the strong interaction between the $|L_6{}^-,v\rangle$ and $|L_6{}^+,c\rangle$ levels, Cohen's nonparabolic model[9] was applied to these bands. By evaluating Cohen's Eqs.

---

[9] M. H. Cohen, Phys. Rev. **121**, 387 (1961).

(11)-(19), we obtain

$$K_0=\frac{\hbar^2\kappa^2}{2m}+\frac{\hbar\boldsymbol{\kappa}}{m}\cdot\sum_{\mu}\frac{\langle L_{61}^-,v|\boldsymbol{\pi}|\mu\rangle\langle\mu|\boldsymbol{\pi}|L_{61}^-,v\rangle}{E(L_6^-,v)-E_\mu}\cdot\frac{\hbar\boldsymbol{\kappa}}{m}, \tag{7}$$

$$K_1=\frac{\hbar^2\kappa^2}{2m}+\frac{\hbar\boldsymbol{\kappa}}{m}\cdot\sum_{\mu}\frac{\langle L_{61}^+,c|\boldsymbol{\pi}|\mu\rangle\langle\mu|\boldsymbol{\pi}|L_{61}^+,c\rangle}{E(L_6^+,c)-E_\mu}\cdot\frac{\hbar\boldsymbol{\kappa}}{m}, \tag{8}$$

$$t=(\hbar\boldsymbol{\kappa}/m)\cdot\langle L_{61}^-,v|\boldsymbol{\pi}|L_{61}^+,c\rangle, \tag{9}$$

$$u=(\hbar\boldsymbol{\kappa}/m)\cdot\langle L_{61}^-,v|\boldsymbol{\pi}|L_{62}^+,c\rangle, \tag{10}$$

$$E_g=E(L_6^+,c)-E(L_6^-,v). \tag{11}$$

Thus the energy relation for the conduction and valence bands becomes

$$\begin{aligned}E_{c,v}=0.9\kappa_z^2-4.64(\kappa_x^2+\kappa_y^2)-0.025\\ \pm\{[1.38\kappa_z^2-18.78(\kappa_x^2+\kappa_y^2)+0.025]^2\\ +0.075\kappa_z^2+0.396(\kappa_x^2+\kappa_y^2)\}^{1/2},\end{aligned} \tag{12}$$

where + and − correspond to c and v, respectively, and $\hbar^2\kappa^2/2m$ has been set equal to unity.

If we denote the function inside the { } brackets in Eq. (12) by f, the relationships

$$\frac{\partial^2 E_{c,v}}{\partial\kappa_i^2}=A_i\mp\tfrac{1}{4}f^{-3/2}\left(\frac{\partial f}{\partial\kappa_i}\right)^2\pm\tfrac{1}{2}f^{-1/2}\frac{\partial^2 f}{\partial\kappa_i^2}\quad(i=x,y,z), \tag{13}$$

result, where $A_x=A_y=-9.28$ and $A_z=1.92$. The effective masses for $\boldsymbol{\kappa}=0$ can be obtained using Eq. (13). Table VIII gives a comparison between the parabolic and nonparabolic effective masses at L along with the g factors. We can see that the nonparabolic effects are substantial for the longitudinal effective mass, while they are practically negligible in transverse directions.

TABLE IV. Composition of the double-group levels used in the **k·p** perturbation.

$$|L_4^-,1\rangle=D|L_4^-(L_{34}')\rangle$$

$$|L_{61}^-,2\rangle=C_1|L_{61}^-(L_{22}')\rangle+C_2|L_{61}^-(L_{34}')\rangle+C_3|L_{61}^-(L_{36}')\rangle$$

$$\begin{aligned}|L_{61}^+,C\rangle=B_1|L_{61}^+(L_{18})\rangle+B_2|L_{61}^+(L_{19})\rangle\\ +B_3|L_{61}^+(L_{110})\rangle+B_4|L_{61}^+(L_{311})\rangle\end{aligned}$$

$$\begin{aligned}|L_{61}^-,v\rangle=A_1|L_{61}^-(L_{21}')\rangle+A_2|L_{61}^-(L_{22}')\rangle\\ +A_3|L_{61}^-(L_{23}')\rangle+A_4|L_{61}^-(L_{34}')\rangle\end{aligned}$$

$$|L_{61}^+,4\rangle=E|L_4^+(L_{311})\rangle$$

$$\begin{aligned}|L_4^+,3\rangle=F_1|L_{61}^+(L_{19})\rangle+F_2|L_{61}^+(L_{110})\rangle\\ +F_3|L_{61}^+(L_{311})\rangle+F_4|L_{61}^+(L_{313})\rangle\end{aligned}$$

TABLE V. Coefficients of spin-orbit mixing for the double-group levels used in **k·p** perturbation.

A_1	−0.081	B_1	−0.072	C_1	−0.126	F_1	−0.130
A_2	−0.987	B_2	−0.985	C_2	0.991	F_2	0.047
A_3	−0.067	B_3	−0.078	C_3	−0.032	F_3	0.990
A_4	−0.125	B_4	0.133	D	−1.000	F_4	0.038
				E	1.000		

TABLE VI. Single-group matrix elements of momentum at L. For computational ease, the given values are for π/m or two times the matrix elements of momentum in a.u.

$M_{18,21}{}^z$	0.861	$M_{21,311}{}^y$	−0.543	$M_{110,34}{}^y$	−0.298
$M_{18,22}{}^z$	0.442	$M_{21,313}{}^y$	0.019	$M_{110,36}{}^y$	−1.062
$M_{18,23}{}^z$	−0.121	$M_{22,311}{}^y$	1.100	$M_{34,311}{}^z$	−0.383
$M_{19,21}{}^z$	−0.299	$M_{22,313}{}^y$	0.003	$M_{34,313}{}^z$	−0.193
$M_{19,22}{}^z$	0.292	$M_{23,311}{}^y$	0.001	$M_{36,311}{}^z$	0.484
$M_{19,23}{}^z$	0.417	$M_{23,313}{}^y$	1.111	$M_{36,313}{}^z$	1.350
$M_{110,21}{}^z$	−0.034	$M_{18,34}{}^y$	−0.174	$M_{34,311}{}^y$	0.833
$M_{110,22}{}^z$	−0.267	$M_{18,36}{}^y$	−0.159	$M_{34,313}{}^y$	−0.426
$M_{110,23}{}^z$	−1.335	$M_{19,34}{}^y$	−1.191	$M_{36,311}{}^y$	0.392
		$M_{19,36}{}^y$	−0.311	$M_{36,313}{}^y$	0.762

TABLE VII. Calculated momentum matrix elements ($\pi'=\pi/m=2\pi$) between the spin-orbit-mixed double-group levels at L in a.u.

$\langle L_{61}^-,v\|\pi_z'\|L_{61}^+,c\rangle$	−0.273	$\langle L_{61}^-,v\|\pi_x'\|L_5^+,3\rangle$	0.521 −0.074i
$\langle L_{61}^-,v\|\pi_x'\|L_{62}^+,c\rangle$	−0.199	$\langle L_{61}^+,c\|\pi_z'\|L_{61}^-,2\rangle$	−0.087
$\langle L_{61}^-,v\|\pi_z'\|L_{61}^+,4\rangle$	0.103	$\langle L_{61}^+,c\|\pi_x'\|L_{62}^-,2\rangle$	0.779
$\langle L_{61}^-,v\|\pi_x'\|L_{62}^+,4\rangle$	−0.719	$\langle L_{61}^+,c\|\pi_x'\|L_4^-,1\rangle$	0.078 −0.569i
$\langle L_{61}^-,v\|\pi_x'\|L_4^+,3\rangle$	−0.074 +0.521i	$\langle L_{61}^+,c\|\pi_x'\|L_5^-,1\rangle$	−0.569 +0.078i

TABLE VIII. Calculated effective masses and g factors at L.

	Parabolic		Nonparabolic			
	m_l^*/m	m_t^*/m	m_l^*/m	m_t^*/m	$\|g_l\|$	$\|g_t\|$
L_6^-,v	−2.381	0.071	−0.513	0.075	7.50	5.62
L_6^+,c	0.427	−0.043	0.258	−0.044	4.07	7.33

The first partial derivatives of $\partial^2E_{c,v}/\partial\kappa_i^2$ are all zero at $\boldsymbol{\kappa}=0$. By looking at the second partial derivatives, we see that except for m_{lv}^*, the rest of the effective masses increase in magnitude as we move away from point L. The E-versus-$\boldsymbol{\kappa}$ surface for the valence band has a saddle shape in the neighborhood of L (Fig. 4). The curvature in the transverse direction is very steep, and thus there should be two maxima very close on either side of L on the face of the Brillouin zone. The same situation exist for the conduction band. Thus the constant-energy surfaces for SnTe are considerably more complicated than they are in the case of the lead chalcogenides.

IV. DEFORMATION POTENTIALS

By using the formalism of Ferreira[10] in treating the strain as a perturbation on the APW energy levels, the deformation potentials at L are calculated for the isotropic strain and three uniaxial strains along [001], [111], and [11$\bar{1}$] directions (Tables IX and X). It is known[4,10] that the isotropic and [111] strain at L do not split any energy levels. However, the rhombohedral [11$\bar{1}$] and tetragonal [001] strains lead to the splitting of the doubly degenerate $L_3^\pm$ levels. Table XI gives the deformation potentials for the double-group levels that form the valence-conduction-band complex at L.

---

[10] L. G. Ferreira, Phys. Rev. **137**, A1601 (1965).

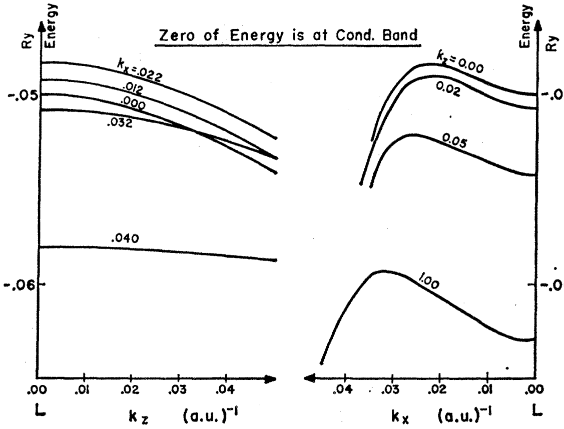

FIG. 4. Energy dispersion for valence band at L in the longitudinal and transverse directions.

V. DISCUSSION AND CONCLUSIONS

A. Band Edges

The calculated energy bands for SnTe indicate that two sets of valence-band maxima occur, one at L and the other in the Σ direction. However, the results of the $\mathbf{k}\cdot\mathbf{p}$ perturbation at L indicate a more complicated situation, namely, that the valence band rises very steeply in energy in the transverse direction. Thus the valence-band energy expanded about L will have a saddle shape, and there would be two true maxima on the face of the Brillouin zone on each side and very close to the point L.

The valence constant-energy surfaces at L, neglecting the nonparabolic effects, will be hyperboloids of revolution about the [111] direction. The conduction band at L has a very similar shape to that of the valence band when inverted. Figure 5 shows the energy-dispersion curves near L for the longitudinal and transverse directions. Burke and Riedl[11] attribute the large value of optical absorption in SnTe in the 0.35–0.42 eV range along with its positive curvature in this region (in contrast to the negative curvature in the case of PbTe,[12] which has simple bands) to the complex shape of the valence band. The present theoretical results indicate such complexity not only for the valence but also for the conduction band.

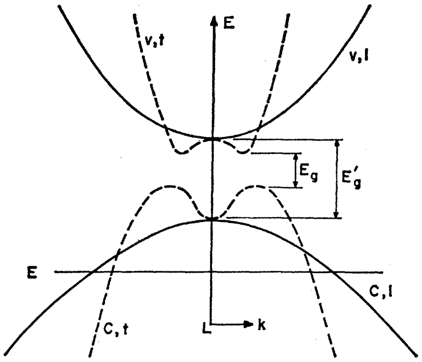

FIG. 5. Conduction- and valence-band edges at L. Solid curves indicate the bands in longitudinal direction [111] and broken curves in the transverse direction (on the face of the Brillouin zone).

There is general experimental agreement[13–15] on the existence of a direct energy gap of about 0.3 eV at 4.2°K and 0.2 eV at 300°K. The calculations give a value of 0.67 eV for E_g' in Fig. 5. Preliminary calculations based on Eq. (12) indicate that E_g is about 0.53 eV. This is in good agreement with experiment, considering the sensitiveness of the gap to the value of the constant potential and the uncertainty in the experimental results.

B. Band Inversion

A significant difference between the energy bands of SnTe at L and those of the lead chalcogenides is due to a reversal of the order of the L_6^- and L_6^+ levels, which correspond to the conduction and valence bands. The first implication of this band inversion is that these two bands will tend to cross each other away from L. However, because of symmetry requirements, this crossing is forbidden, and the avoidance of crossing leads to the two maxima off L. The second implication is that the deformation potential for the gap between these two bands will change sign from that of the lead chalcogenides. This is shown theoretically by the fact that D_{ISO} (cond.−val.) at L for SnTe is −8.68 eV while for the others,[4,10] it ranges from 11.55 to 17.24 eV. Although, in the case of SnTe, this calculated value should be different from the true deformation potential for minimum gap E_g. The band inversion was first pre-

TABLE IX. Matrix elements of isotropic and [111] uniaxial strains between the single-group states at L in eV.

Single-group states	Iso.	[111]	Single-group states	Iso.	[111]
L_{21}',L_{21}'	4.38	− 1.08	L_{18},L_{18}	9.53	− 0.04
L_{22}',L_{22}'	− 6.70	4.06	L_{19},L_{19}	−15.54	1.89
L_{23}',L_{23}'	−22.81	−11.35	L_{110},L_{110}	−23.86	−13.97
L_{21}',L_{22}'	0	− 0.57	L_{18},L_{19}	0	− 1.51
L_{21}',L_{23}'	0	6.13	L_{18},L_{110}	0	2.18
L_{22}',L_{23}'	0	− 6.17	L_{19},L_{110}	0	8.28
L_{34}',L_{34}'	− 4.52	3.72	L_{311},L_{311}	− 4.62	2.28
L_{36}',L_{36}'	−16.36	− 9.40	L_{313},L_{313}	−16.73	− 8.45
L_{34}',L_{36}'	0	3.16	L_{311},L_{313}	0	− 6.28

---

[11] J. R. Burke, Jr. and H. R. Riedl (private communication).

[12] W. W. Scanlon, in *Solid State Physics*, edited by F. Seitz and D. Turnbull (Academic Press Inc., New York, 1959), Vol. 9, p. 115.

[13] L. Esaki and P. J. Stiles, Phys. Rev. Letters **16**, 1108 (1966).

[14] R. B. Schoolar, H. R. Riedl, and J. R. Dixon, Solid State Commun. 4, 423 (1964).

TABLE X. Matrix elements of [11$\bar{1}$] and [001] uniaxial strains between single-group states at L in eV.

Single-group states	R	T	Single-group states	R	T
$L_2^-(L_{21}'),L_2^-(L_{22}')$	6.09	4.42	$L_1^+(L_{18}),L_1^+(L_{19})$	− 2.72	−2.41
$L_2^-(L_{21}'),L_2^-(L_{23}')$	1.01	2.29	$L_1^+(L_{18}),L_1^+(L_{110})$	− 1.17	−0.33
$L_2^-(L_{22}'),L_2^-(L_{23}')$	− 2.74	− 3.60	$L_1^+(L_{19}),L_1^+(L_{110})$	4.17	5.20
$L_2^-(L_{21}'),L_2^-(L_{34}')$	− 2.48	− 6.26	$L_1^+(L_{18}),L_1^+(L_{311})$	− 0.29	−3.67
$L_2^-(L_{21}'),L_2^-(\mathrm{A}_{36}')$	− 6.21	2.12	$L_1^+(L_{18}),L_1^+(L_{313})$	0.88	0.67
$L_2^-(L_{22}'),L_2^-(L_{34}')$	4.53	6.31	$L_1^+(L_{19}),L_1^+(L_{311})$	− 4.36	−7.26
$L_2^-(L_{22}'),L_2^-(L_{36}')$	5.44	− 1.74	$L_1^+(L_{19}),L_1^+(L_{313})$	8.50	−1.27
$L_2^-(L_{23}'),L_2^-(L_{34}')$	− 2.95	− 1.85	$L_1^+(L_{110}),L_1^+(L_{311})$	− 4.25	−0.40
$L_2^-(L_{23}'),L_2^-(L_{36}')$	13.73	− 5.95	$L_1^+(L_{110}),L_1^+(L_{313})$	−12.78	6.42
$L_1^-(L_{34}'),L_1^-(L_{34}')$	− 0.80	2.09	$L_2^+(L_{311}),L_2^+(L_{311})$	− 1.32	1.19
$L_1^-(L_{34}'),L_1^-(L_{36}')$	0.09	4.41	$L_1^+(L_{311}),L_1^+(L_{313})$	− 2.27	1.77
$L_1^-(L_{36}'),L_1^-(L_{36}')$	4.66	−10.14	$L_2^+(L_{313}),L_2^+(L_{313})$	3.87	−9.14
$L_2^-(L_{34}'),L_2^-(L_{36}')$	− 1.98	− 1.27	$L_2^+(L_{311}),L_2^+(L_{313})$	0.99	−5.86

dicted by Dimmock *et al.*[16] on the basis of data from luminescence at 12°K, optical absorption at 300°K in $\mathrm{Pb}_x\mathrm{Sn}_{1-x}\mathrm{Te}$, and tunnelling in SnTe at 4.2 and 300°K. Further experimental evidence is supplied by Dixon and Bis[17] as a result of resistivity and Hall coefficient measurements on $\mathrm{Pb}_x\mathrm{Sn}_{1-x}\mathrm{Te}$ alloys as a function of temperature. They obtain breaks in the resistivity curves at temperatures which are in agreement with temperatures predicted for band crossing as a function of composition.

C. Two-Band Model for Valence Band

A two-valence-band model for SnTe, was proposed by Allgaier and Scheie[18] to explain the temperature dependence of the Hall coefficient. A great deal of subsequent experimental results[19–22] have been accumulated that point to the validity of this model. This behavior of the Hall coefficient, which reaches a peak at about 700°K, has been interpreted by Andriev[22] as a two-band effect including interband scattering. Further experimental support comes from the carrier-concentration dependence of the thermoelectric coefficient and of the ratio R_T/R_{77}.[20,21,23] A very abrupt rise in the thermoelectric power α occurs at the same carrier concentration at which there is a kink in the R_T/R_{77} curve. This can be attributed to the entry of the Fermi level from one band into another, i.e., a break in the density of states.[22] Some of the above behavior could be explained on the basis of a single nonparabolic band. However, the absence of similar behavior of $R(T)$ in n-type lead chalcogenides, in view of the similarity of their valence- and conduction-band shapes at L, renders this explanation implausible.

The theoretical band calculation (Fig. 1) shows a second set of apparent valence maxima in the [110] direction that may provide the second band of the two-band model, although in the absence of a $\mathbf{k}\cdot\mathbf{p}$ perturbation for this maxima, we cannot make a detailed analysis. Tsu *et al.*[24] have identified the second band as a lower-lying valence band at L with a separation of 0.34 eV. However, this does not agree with the calculated bands which give the separation at L a lower limit of 0.84 eV. Furthermore, their symmetry assignments to the band do not agree with any of the theoretical studies of SnTe or the lead chalcogenides. The results of the nonparabolic approximation given in Sec. III indicate that even in a two-band model, one cannot safely neglect the nonparabolic effect in the bands at L, especially since the correction is sizable in the transverse direction (Table VIII) and since the maxima occur in this direction.

TABLE XI. Deformation potentials in eV, for the spin-orbit mixed double-group levels that make the valence-conduction band complex at L.

Spin-orbit mixed-double-group level	D_{iso}	D_{111}	$D_{11\bar{1}}$	D_{001}	D_u	D_d
$\lvert L_4^-,L_5^-,1\rangle$	− 4.52	3.72	−3.25	−1.51	7.84	−4.12
$\lvert L_6^-,2\rangle$	− 4.57	3.50	−3.20	−1.64	7.54	−4.04
$\lvert L_6^+,c\rangle$	−15.33	−0.21	−8.04	−6.08	7.35	−7.56
$\lvert L_6^-,v\rangle$	− 6.65	3.10	−3.65	−1.96	7.98	−4.88
$\lvert L_4^+,L_5^+,3\rangle$	− 4.62	2.28	−3.31	−1.54	5.73	−3.45
$\lvert L_6^+,4\rangle$	− 4.91	1.62	−3.54	−1.86	4.89	−3.27

---

[15] B. F. Bilenkii, A. G. Mikolaichuk, and D. M. Freik, Phys. Status Solidi **28**, K5 (1968).

[16] J. O. Dimmock, J. Melngailis, and A. J. Strauss, Phys. Rev. Letters **16**, 1193 (1966).

[17] J. R. Dixon and R. F. Bis, Phys. Rev. **176**, 942 (1968).

[18] R. S. Allgaier and P. O. Scheie, Bull. Am. Phys. Soc. **6**, 436 (1961).

[19] R. S. Allgaier and B. B. Houston, Jr., in *Proceedings of the International Conference on the Physics of Semiconductors, Exeter* (The Institute of Physics and the Physical Society, London, 1962), p. 172.

[20] R. F. Brebrick and A. J. Strauss, Phys. Rev. **131**, 104 (1963).

[21] V. I. Kaidanov, I. A. Chernik, and B. A. Efimova, Fiz. Tekh. Poluprovodnikov **1**, 869 (1967) [English transl.: Soviet Phys.—Semiconductors **1**, 723 (1967)].

[22] A. A. Andreev, Fiz. Tverd. Tela **9**, 1560 (1967) [English transl.: Soviet Phys.—Solid State **9**, 1232 (1967)].

[23] R. S. Allgaier (private communication).

[24] R. Tsu, W. E. Howard, and L. Esaki, Phys. Rev. **172**, 779 (1968).

Shubnikov–de Haas measurements[25,26] have shown the complicated nature of the primary valence band by the large number of cross sections observed, and seem to confirm the existence of the second valence band, since a new cross section appears at higher carrier concentrations. However, the symmetry of this cross section does not seem to point to a {110} surface.

The nonsimple valence band, high carrier concentration ($\sim 10^{20}$ cm^{-3}), and high static dielectric constant of 1200 ± 200 [27] could be responsible for the appearance of superconductivity in SnTe,[28] according to Cohen's[29] theory of superconductivity in multivalleyed degenerate semiconductors. The existence of the large number of valleys (20 valleys, if the $\sum$ maxima are taken into account) should enhance the conditions of superconductivity by providing a large number of states at the Fermi level for intervalley carrier scattering, especially since these transitions, as a consequence of large momentum transfer, are less screened than the intravalley processes. Furthermore, the transition temperature rises with increasing carrier concentration, which further supports the above conclusions.

ACKNOWLEDGMENTS

I am indebted to Professor George W. Pratt, Jr., for originally suggesting this research. Thanks are due to Dr. M. A. Gilleo and Dr. P. T. Bailey for helpful discussions. Special thanks are due to Dr. R. S. Allgaier and Dr. J. R. Burke, Jr., for extremely helpful discussions, suggestions, and for making certain unpublished results available. I am grateful to Dr. J. W. Connolly and Dr. Frank Arlinghaus for some computer programs. Acknowledgment is made of use of the computation facilities of the Management Information and Systems Department of Monsanto.

---

[25] J. R. Burke, Jr., R. S. Allgaier, and B. B. Houston, Jr., Phys. Rev. Letters **14**, 360 (1965).

[26] J. R. Burke, Jr., B. B. Houston, Jr., H. T. Savage, J. Babiskin, and P. G. Siebenmann, J. Phys. Soc. Japan Suppl. **21**, 384 (1966).

[27] G. S. Pawley *et al.*, Phys. Rev. Letters **17**, 753 (1966).

[28] R. A. Hein *et al.*, in *Proceedings of the Ninth International Conference on Low-Temperature Physics, Columbus, Ohio*, edited by J. G. Daunt *et al.* (Plenum Press, Inc., New York, 1965), p. 604.

[29] M. L. Cohen, Phys. Rev. **134**, A511 (1964).

PHYSICAL REVIEW VOLUME 182, NUMBER 3 15 JUNE 1969

Local and Nonlocal Magnetoplasma Effects in *n*-Type Lead Telluride*

S. Perkowitz†
Laboratory for Research on the Structure of Matter and Physics Department,
University of Pennsylvania, Philadelphia, Pennsylvania 19104

(Received 18 November 1968)

Measurements of the derivative of the microwave absorption coefficient as a function of static magnetic field **H** have been carried out in high-mobility (1.0×10^6 cm^2/V sec) *n*-type lead telluride at 70 GHz and 4.2°K. The measurements were taken in the Voigt ($\mathbf{q}_0 \perp \mathbf{H}$, where $\mathbf{q}_0$ is the incident radiation wave vector) and Faraday ($\mathbf{q}_0 \| \mathbf{H}$) configurations, as well as in intermediate geometries, where a mixed Voigt-Faraday situation applied. The sample surface, a {110} plane, was fixed perpendicular to $\mathbf{q}_0$, and **H** was rotated in a {100} plane which contained $\mathbf{q}_0$. The data were analyzed using well-known local theory and a simplified nonlocal theory for the Azbel-Kaner and Doppler-shifted cyclotron resonances. The observed local magnetoplasma effects agreed with those predicted from the ⟨111⟩-ellipsoid model and included the hybrid resonance which has not been previously reported in lead telluride. The values deduced for the transverse mass m_t and the mass ratio $K = m_l/m_t$ were $m_t/m_0 = 0.043 \pm 0.04$ and $K = 9.7 \pm 1.4$ at a carrier concentration of 8.1×10^{17} cm^{-3}. Two weak, low-field resonances were identified as the first and second Azbel-Kaner subharmonics of a tilted-orbit cyclotron resonance. The values of the magnetic field at which the resonances and dielectric anomalies were observed in the Faraday geometry were shifted 4–19% relative to the corresponding values in the Voigt geometry, and some of these shifts agreed with the predictions of the simple Doppler-shift theory. Analysis of the Voigt dielectric-anomaly data gave a value of 10^4 for the static part of the lattice dielectric constant. A similar value has been obtained in microwave-helicon experiments, while other methods of determination have given values near 400.

1. INTRODUCTION

The free-charge carriers of a solid form a plasma which in the presence of electromagnetic radiation and a static magnetic field sustains the electromagnetic waves known as magnetoplasma modes. These modes exhibit a variety of interesting properties which depend upon the band structure of the material and the degree of nonlocality in the internal current–electric-field relation. In the limit where the current-

---

[*] Based upon a dissertation by the author submitted to the Physics Department of the University of Pennsylvania in partial fulfillment of the requirements for the Ph.D. degree. Work supported by the U. S. Office of Naval Research under Contract No. NONR 551(51) and the dissertation has been issued as Technical Report No. AD 652 620.

[†] Present address: General Telephone and Electronics Laboratories, Inc., Bayside, N. Y. 11360.